Catalysis Science & Technology

ROYAL SOCIETY OF CHEMISTRY

PAPER

View Article Online
View Journal | View Issue

Cite this: *Catal. Sci. Technol.*, 2021, **11**, 2316

Outstanding performance of CuO/Fe–Ti spinel for Hg^0 oxidation as a co-benefit of NO abatement: significant promotion of Hg^0 oxidation by CuO loading†

Pengxiang Sun, Jian Mei, * Chang Wang, Zhen Ding, Qianqian Hong and Shijian Yang

Received 25th October 2020,
Accepted 17th January 2021

DOI: 10.1039/d0cy02081h

rsc.li/catalysis

Conversion of gaseous Hg^0 to soluble Hg^{2+} using selective catalytic reduction (SCR) catalysts with gaseous HCl as an oxidant as a co-benefit of NO abatement is widely used for resolving Hg pollution from coal-burning power plants. Nevertheless, the performances of conventional V_2O_5–WO_3/TiO_2 for NO abatement and Hg^0 oxidation are unsatisfactory. In this study, CuO/Fe–Ti spinel was exploited as a novel and high-activity catalyst for the simultaneous removal of NO and Hg^0. The outstanding SCR activity and high N_2 selectivity of Fe–Ti spinel did not distinctly decrease after CuO loading; thus, CuO/Fe–Ti spinel achieved efficient NO reduction. Although Hg^0 physical adsorption onto Fe–Ti spinel was slightly suppressed after CuO loading, the Cl* radical formation was appreciably promoted as both HCl adsorption and the conversion of adsorbed Cl^- to Cl* radicals were promoted. Hence, the Hg^0 oxidation activity of Fe–Ti spinel was appreciably improved after CuO loading, and the rate of Hg^0 oxidation for CuO/Fe–Ti spinel reached approximately 6.8–8.7 μg g^{-1} min^{-1}, which was better than those of most other SCR catalysts. In summary, CuO/Fe–Ti spinel shows great promise as an SCR catalyst for Hg^0 oxidation as a co-benefit of NO abatement from coal-burning flue gas (CFG).

1. Introduction

Owing to the increasing incidence of Hg pollution, a legally binding international convention (*i.e.*, the Minamata Convention on Mercury) aiming at reducing Hg emissions was signed in 2013.[1–3] Coal-burning power plants are momentous anthropogenic Hg emission sources; therefore, they are rigorously constrained by this convention.[4,5] Three types of Hg species are present in coal-burning flue gas (CFG), *i.e.*, particulate (Hg^p), elemental (Hg^0), and oxidized (Hg^{2+}) mercury.[6,7] A dust collector and desulfurizer can effectively remove Hg^p and Hg^{2+} in coal-burning power plants, respectively.[8,9] However, since Hg^0 is highly volatile and insoluble, it is hard to be removed using these devices.[10] Hence, reducing the emissions of Hg^0 is critical for controlling Hg pollution from coal-burning power plants.

Conversion of gaseous Hg^0 to soluble Hg^{2+} using selective catalytic reduction (SCR) catalysts with gaseous HCl as an oxidant as a co-benefit of NO abatement could be a viable approach to reduce the emissions of Hg^0 from CFG.[11–13] However, the ability of conventional V_2O_5–WO_3/TiO_2 to oxidize Hg^0 is unsatisfactory, and its activity is closely related to the operating conditions, for instance the HCl content, temperature, and space velocity.[14,15] The components of flue gas (*i.e.*, H_2O, SO_2, NH_3, and NO) also interfere with Hg^0 oxidation on conventional V_2O_5–WO_3/TiO_2.[16] For example, the injection of NH_3 notably suppresses Hg^0 oxidation on conventional V_2O_5–WO_3/TiO_2.[17,18] Hence, some researchers attempted to improve the Hg^0 oxidation activity of conventional V_2O_5–WO_3/TiO_2 through modification. Yan *et al.* found that RuO_2 loading not only appreciably improved the oxidation ability of V_2O_5–WO_3/TiO_2, but also greatly promoted the occurrence of the Deacon reaction; thus, RuO_2-doped V_2O_5–WO_3/TiO_2 displayed satisfactory activity for Hg^0 oxidation.[19] Chen *et al.* observed that $CuCl_2$ loading provided more activated Cl species in V_2O_5–WO_3/TiO_2 for Hg^0 oxidation, appreciably improving the Hg^0 oxidation activity of V_2O_5–WO_3/TiO_2.[20] However, the SCR activity and N_2 selectivity of these modified V_2O_5–WO_3/TiO_2 catalysts are insufficient, which severely limits their potential applications in NO abatement from CFG.

Recently, various novel and high-activity SCR catalysts have been exploited to substitute for conventional V_2O_5–WO_3/

School of Environment and Civil Engineering, Jiangnan University, Wuxi, 214122, P. R. China. E-mail: jsjhmj@126.com

† Electronic supplementary information (ESI) available. See DOI: 10.1039/d0cy02081h

TiO_2 for NO abatement from CFG. Zhu *et al.* found that $Cu_{0.25}$–$Nb_{0.85}$ could not only completely convert NO in a broad temperature window (*i.e.*, 180–330 °C), but also achieved a N_2 selectivity of approximately 100%, which was predominantly due to the presence of redox recycling (*i.e.*, $Cu^{2+} + Nb^{4+} \leftrightarrow Cu^{+} + Nb^{5+}$) and the abundant acid sites on the surface.[21] Wu *et al.* observed that the dispersion of MnO_x on γ-Al_2O_3 and the formation of Mn^{3+} on MnO_x/γ-Al_2O_3 were both appreciably improved by Mo addition; thus, Mo–Mn/γ-Al_2O_3 exhibited excellent SCR performance across a wide temperature range (*i.e.*, 150–300 °C).[22] Niu *et al.* suggested that $Cu_{0.02}Fe_{0.2}W_{0.02}TiO_x$ had excellent NO conversion ability, high N_2 selectivity, a wide temperature window (*i.e.*, 235–520 °C), and strong tolerance to SO_2 and H_2O, which were predominantly attributed to the sufficient acidity and combined effect of redox.[23] However, the Hg^0 oxidation activities of these novel and high-performance SCR catalysts are not satisfactory, and it is difficult to meet the demand for Hg^0 removal as a co-benefit of NO abatement. Hence, novel SCR catalysts for Hg^0 oxidation as a co-benefit of NO abatement urgently need to be developed.

We previously demonstrated that Fe–Ti spinel could achieve outstanding SCR activity and high N_2 selectivity, while its Hg^0 oxidation activity was moderate.[24] However, our previous study on Hg^0 oxidation on CuO/TiO_2 found that CuO exhibited excellent Hg^0 oxidation activity.[25] In this study, CuO was loaded on Fe–Ti spinel to further improve its Hg^0 oxidation performance, and the mechanism by which CuO loading promotes Hg^0 oxidation on Fe–Ti spinel was deeply investigated in detail. Hg^0 oxidation on CuO/Fe–Ti spinel predominantly followed the Langmuir–Hinshelwood mechanism (*i.e.*, physically adsorbed Hg^0 is oxidized by Cl* radicals to $HgCl_2$), and its rate was dominantly dependent upon the amounts of surface Cl* radicals and physically adsorbed Hg^0. Although Hg^0 physical adsorption onto Fe–Ti spinel was slightly suppressed after CuO loading, the formation of Cl* radicals was appreciably promoted due to the promotion of both HCl adsorption and the conversion of adsorbed Cl^- to Cl* radicals. Hence, CuO/Fe–Ti spinel displayed outstanding performance in Hg^0 oxidation. It also displayed glorious SCR activity and high N_2 selectivity. Therefore, CuO/Fe–Ti spinel shows great promise as an SCR catalyst for the effective removal of Hg^0 as a co-benefit of NO abatement from CFG.

2. Experimental section

2.1 Catalyst synthesis

Fe_2TiO_4 was synthesized following a co-precipitation method with precursors of ferrous sulfate and titanous sulfate (both provided by Sinopharm Group Chemical Reagent Co. LTD, analytical reagent),[26] and was then calcined at 500 °C for 180 min to obtain Fe–Ti spinel. Finally, 1 wt% of CuO was loaded onto Fe–Ti spinel *via* an impregnation method with a precursor of copper nitrate (provided by Sinopharm Group Chemical Reagent Co. LTD, analytical reagent), followed by calcination at 500 °C for 180 min to obtain CuO/Fe–Ti spinel. For comparison, V_2O_5–WO_3/TiO_2 was synthesized following an impregnation method with precursors of ammonium metavanadate and ammonium tungstate (both provided by Sinopharm Group Chemical Reagent Co. LTD, analytical reagent), and the loading contents of V_2O_5 and WO_3 were 1 wt% and 10 wt%, respectively.[27]

2.2 Characterization

The crystal structure, Brunauer–Emmett–Teller (BET) surface area, surface properties, and redox ability were determined using an X-ray diffractometer (XRD, Bruker-AXS D8 Advance), physical adsorption analyzer (Quantachrome 2200e), X-ray photoelectron spectroscope (XPS, ThermoFisher Scientific ESCALAB 250 Xi), and chemical adsorption analyzer (Autochem II 2920), respectively. The thermal stability of adsorbed Hg species was assessed based on the temperature programmed desorption of Hg^0 (Hg-TPD).

2.3 Activity evaluation

The activity of the catalyst in Hg^0 oxidation was assessed using a packed-bed reaction system (Fig. S1†) at 250–450 °C with a mass hourly space velocity (MHSV) of 6.0×10^6 $cm^3\ g^{-1}\ h^{-1}$ (catalyst weight was 5 mg and gas flow rate was 500 mL min^{-1}). Meanwhile, the performances for NO abatement and Hg^0 adsorption were also assessed using the packed-bed reaction system at 250–450 °C with a MHSV of 6.0×10^4 and 6.0×10^5 $cm^3\ g^{-1}\ h^{-1}$, respectively. The simulated CFG generally included 90 μg m^{-3} Hg^0, 10 ppm HCl, 5% O_2, chemical components (*i.e.*, 8% H_2O, 500 ppm SO_2, 500 ppm NH_3, and 500 ppm NO when used), and N_2 balance. A stable concentration of Hg^0 was provided by an Hg permeation tube (provided by Greencalm Instruments of Suzhou, China) and the Hg^0 concentration was adjusted by changing the temperature of the water bath. The amount of Hg^0 was monitored based on a cold vapor atomic adsorption spectrophotometer (CVAAS, Lumex RA-915M). The amount of total Hg (Hg^t) was acquired through reducing Hg^{2+} to Hg^0 with a $SnCl_2$ solution. The amount of Hg^{2+} was then determined *via* deducting the amount of Hg^0 from that of Hg^t. An industrial gas system (IGS) analyzer infrared spectrometer from ThermoFisher Scientific ANTARIS was used to monitor the NO and N_2O amounts.

3. Results and discussion

3.1 Performances for SCR and Hg^0 oxidation

The SCR performances of Fe–Ti and CuO/Fe–Ti spinel under normal SCR conditions (*i.e.*, H_2O, SO_2, NH_3, and NO were present) are compared in Fig. 1a. Fe–Ti spinel displayed outstanding SCR activity at 300–450 °C, and the NO removal efficiencies were all approximately equivalent to 100%. Meanwhile, the N_2O selectivity of Fe–Ti spinel was also very low (<4%), suggesting that Fe–Ti spinel had high N_2 selectivity. Following CuO loading, the NO removal efficiency

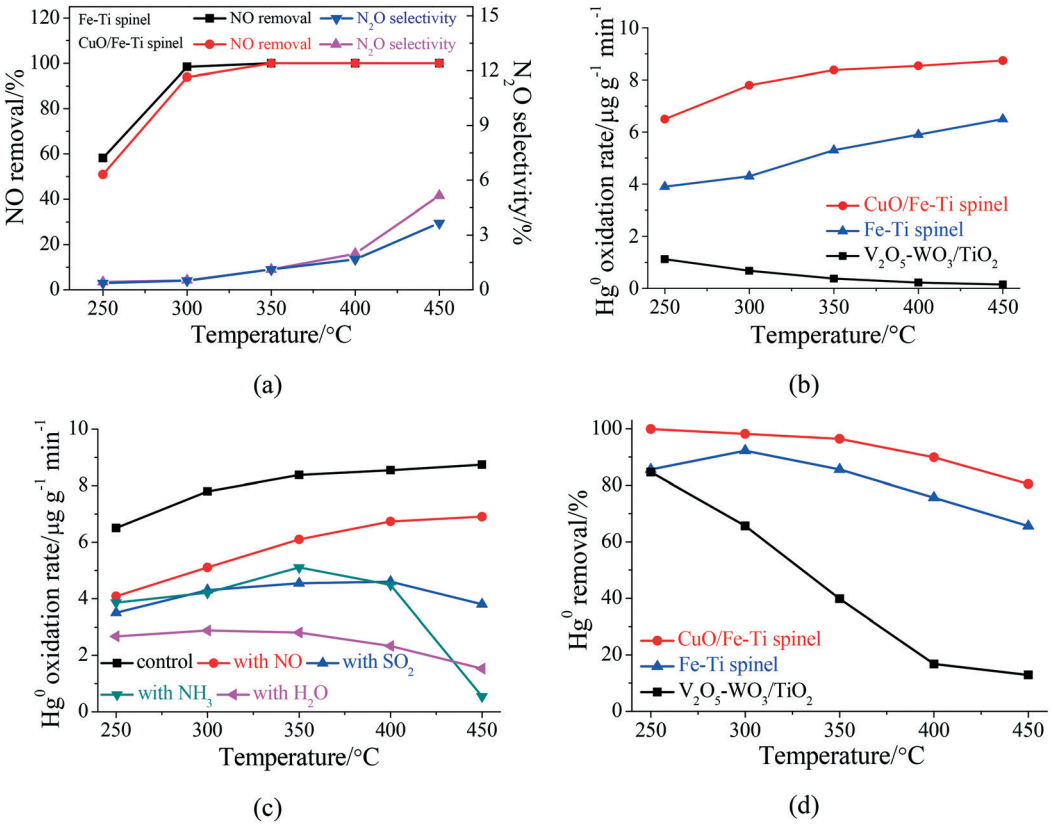

Fig. 1 (a) NO removal efficiency and N_2O selectivity of Fe–Ti and CuO/Fe–Ti spinel under normal SCR conditions. Operating conditions: catalyst weight = 500 mg and MHSV = 6.0×10^4 cm^3 g^{-1} h^{-1}. (b) Rates of Hg^0 oxidation on V_2O_5–WO_3/TiO_2, Fe–Ti, and CuO/Fe–Ti spinel. (c) Influences of the components of flue gas on Hg^0 oxidation on CuO/Fe–Ti spinel. (d) Hg^0 removal efficiencies of V_2O_5–WO_3/TiO_2, Fe–Ti, and CuO/Fe–Ti spinel under normal SCR conditions. Operating conditions: catalyst weight = 500 mg and MHSV = 6.0×10^4 cm^3 g^{-1} h^{-1}.

of Fe–Ti spinel slightly decreased at 300 °C, but it still reached 94%. Meanwhile, the NO removal efficiency of Fe–Ti spinel barely varied at 350–450 °C after CuO loading. Although the N_2O selectivity of Fe–Ti spinel slightly increased at 400–450 °C after CuO loading, it was still below 5%. These results suggest that the outstanding SCR activity and high N_2 selectivity of Fe–Ti spinel at 300–450 °C did not distinctly decrease after CuO loading; thus, CuO/Fe–Ti spinel achieved efficient NO reduction.

The Hg^0 oxidation activities of Fe–Ti and CuO/Fe–Ti spinel are compared in Fig. 1b. The activity of Fe–Ti spinel was moderate at 250–450 °C, and its Hg^0 oxidation rate was approximately 3.9–6.5 μg g^{-1} min^{-1}. After CuO loading, the Hg^0 oxidation rate increased to approximately 6.5–8.7 μg g^{-1} min^{-1}. This suggests that CuO/Fe–Ti spinel displayed outstanding Hg^0 oxidation activity, which also exceeded those of V_2O_5–WO_3/TiO_2 (Fig. 1b) and most other SCR catalysts.[28–30]

H_2O, SO_2, NH_3, and NO are the permanent components of flue gas in SCR units; therefore, their influences on Hg^0 oxidation by CuO/Fe–Ti spinel were explored. Fig. 1c shows that the Hg^0 oxidation rates of CuO/Fe–Ti spinel all remarkably decreased when H_2O, SO_2, NH_3, and NO were introduced, suggesting that all these gases interfered with Hg^0 oxidation on CuO/Fe–Ti spinel. However, a desired removal efficiency of Hg^0 (>95%) was still achieved by CuO/Fe–Ti spinel under normal SCR conditions at 250–350 °C, which was also apparently larger than those of Fe–Ti spinel and V_2O_5–WO_3/TiO_2 (Fig. 1d). Furthermore, Fig. S2† shows that CuO/Fe–Ti spinel exhibited excellent stability during the simultaneous removal of Hg^0 and NO, and the Hg^0 and NO removal efficiencies and N_2O selectivity were stable at approximately 96%, 100%, and 1.6% under normal SCR conditions for 10 h at 350 °C, respectively. These results suggest that CuO/Fe–Ti spinel could simultaneously remove Hg^0 and NO under normal SCR conditions, and it can be applied in SCR units to replace conventional V_2O_5–WO_3/TiO_2 for controlling the emissions of NO and Hg^0 from CFG.

3.2 Characterization

3.2.1 XRD and BET. The XRD pattern of Fe–Ti spinel (Fig. 2) was in agreement with the standard card of maghemite (JCPDS: 39-1346), meaning that synthetic Fe–Ti spinel was present as a spinel structure. The XRD pattern did not significantly change after CuO loading, and no peaks corresponding to any copper oxides appeared (Fig. 2). Therefore, the spinel structure was not destroyed, and copper oxides may be highly dispersed on Fe–Ti spinel.

The BET surface areas of Fe–Ti and CuO/Fe–Ti spinel were 47.1 and 39.3 m^2 g^{-1}, respectively.

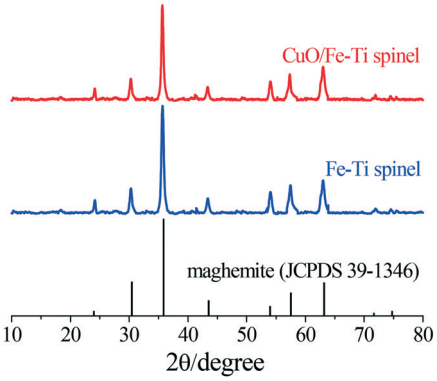

Fig. 2 XRD patterns of Fe–Ti and CuO/Fe–Ti spinel.

3.2.2 XPS. The Fe $2p_{3/2}$ binding energies for Fe–Ti spinel were dominantly located at 710.6 and 712.2 eV (Fig. 3a) due to Fe^{3+} and Fe^{3+}–OH, respectively.[31] The Ti 2p binding energies for Fe–Ti spinel were dominantly located at 458.6 and 464.3 eV (Fig. 3b) due to Ti^{4+}.[32] The O 1s binding energies for Fe–Ti spinel were dominantly located at 530.1 and 531.6 eV (Fig. 3c) due to the lattice O and O in –OH, respectively.[33] The Fe 2p, Ti 2p, and O 1s spectra of CuO/Fe–Ti spinel (Fig. 3d–f) fitted with those of Fe–Ti spinel. However, a new Cu $2p_{3/2}$ binding energy at 933.2 eV was observed for CuO/Fe–Ti spinel (Fig. 3g), which was related to Cu^{2+}.[34]

After 10 h of Hg^0 oxidation, the Fe 2p, Ti 2p, O 1s, and Cu $2p_{3/2}$ spectra of CuO/Fe–Ti spinel did not vary significantly (Fig. S3†). However, two binding energies dominantly located at 198.4 and 199.9 eV, both corresponding to Cl^-,[16,25] were observed for CuO/Fe–Ti spinel (Fig. 3h), meaning that HCl can adsorb onto CuO/Fe–Ti spinel during the oxidation of Hg^0. Moreover, no peak corresponding to Hg 4f appeared for CuO/Fe–Ti spinel after 10 h of Hg^0 oxidation (Fig. 3i).

3.2.3 H_2-TPR. There were two remarkable reduction peaks in the H_2-TPR profile of Fe–Ti spinel (Fig. 4). The sharp peak at 473 °C was attributed to the reduction of $(Fe_2Ti)_{1-\delta}O_4$ to Fe_2TiO_4, while the wide peak located at higher temperatures was due to the reduction of Fe_2TiO_4 to Fe^0 and TiO_2.[35] The weak peak at 605 °C might be related to the transition phase of $FeTiO_3$ or $FeTi_2O_5$.[26] After CuO loading, the reduction of Fe–Ti spinel scarcely varied, while a new reduction peak at 361 °C was observed (Fig. 4). Since the electron transfer between the cycles of Cu^{2+}/Cu^+ and Fe^{2+}/Fe^{3+} easily occurred when highly dispersed CuO was present on Fe–Ti spinel, there was a synergistic effect between Cu and Fe species on CuO/Fe–Ti spinel.[36] Therefore, the reduction peak at 361 °C might result from the coupled reduction of Cu^{2+} and Fe^{3+}, resulting in a smaller reduction peak at 473 °C. Since the first reduction peak of CuO/Fe–Ti spinel was approximately 112 °C lower than that of Fe–Ti spinel, CuO loading appreciably improved the oxidation ability of Fe–Ti spinel.

3.3 Hg balance

The amount of Hg^0 decreased dramatically from 90 to 26 μg m^{-3} after the introduction of Hg^0 + HCl + O_2 into CuO/Fe–Ti spinel at 250 °C, and then stabilized at 26 μg m^{-3} for 120 min (Fig. 5a). Furthermore, the Hg^t amount decreased dramatically to 73 μg m^{-3}, and then recovered to 90 μg m^{-3} within 10 min (Fig. 5a). Hence, a stable amount of Hg^{2+} (74 μg m^{-3}) was observed at the outlet (Fig. 5a). By integrating the Hg^t breakthrough curve, the content of Hg species adsorbed on CuO/Fe–Ti spinel was obtained, with a value of approximately 0.04 μg, which was equal to that of desorbed Hg^t (Fig. 5b). This accounted for only 1.0% of the reduced Hg^0. Meanwhile, no peak corresponding to Hg 4f appeared on CuO/Fe–Ti spinel after 10 h of Hg^0 oxidation (Fig. 3i). Therefore, little Hg adsorbed onto CuO/Fe–Ti spinel during Hg^0 oxidation, and most of Hg^0 was oxidized to Hg^{2+}.

3.4 Transient reaction

Fig. 6a shows the amounts of Hg^0, Hg^t, and Hg^{2+} at the outlet during the introduction of Hg^0 + O_2 into CuO/Fe–Ti spinel pretreated with O_2 + HCl at 250 °C. After 90 μg m^{-3} of Hg^0 + O_2 was introduced into CuO/Fe–Ti spinel pretreated with O_2 + HCl, the amount of Hg^0 at the outlet increased dramatically to 43 μg m^{-3}, and it then slowly increased to 48 μg m^{-3} within 120 min. Moreover, the Hg^t amount in the outlet was maintained at 90 μg m^{-3}. Hence, 47 μg m^{-3} of Hg^{2+} at the outlet was observed in the initial stage, which then slowly decreased to 42 μg m^{-3} within 120 min. Therefore, gaseous or adsorbed Hg^0 could be oxidized by gaseous Cl_2 or adsorbed HCl to $HgCl_2$. With the increase of the Hg^0 amount to 180 and 270 μg m^{-3}, the initial Hg^{2+} amounts at the outlet increased by approximately 57% and 119%, respectively (Fig. 6b). However, the downward trend of the Hg^{2+} amount became more noticeable with an increase of the Hg^0 amount (Fig. 6b).

The initial amount of Hg^{2+} at the outlet increased by approximately 28% when 90 μg m^{-3} of Hg^0 + O_2 was introduced into CuO/Fe–Ti spinel pretreated with O_2 + HCl at 250 °C (Fig. 6c). Hence, Hg^{2+} formation on Fe–Ti spinel was appreciably promoted after CuO loading, which was the same as the result presented in Fig. 1b. Meanwhile, the downward trend of the Hg^{2+} amount on CuO/Fe–Ti spinel was more gradual than that on Fe–Ti spinel (Fig. 6c). Therefore, appreciably more Hg^{2+} formed on CuO/Fe–Ti spinel than Fe–Ti spinel.

Since H_2O, SO_2, NH_3, and NO all remarkably interfered with Hg^0 oxidation on CuO/Fe–Ti spinel (Fig. 1c), their interferences with Hg^{2+} formation during the introduction of Hg^0 + O_2 into CuO/Fe–Ti spinel pretreated with O_2 + HCl at 250 °C were investigated. Fig. 7a shows that the amounts of Hg^{2+} formed all distinctly decreased when H_2O, SO_2, NH_3, and NO were introduced with O_2 + HCl during the pretreatment process. Fig. 7b shows that the decreasing tendencies of the Hg^{2+} amounts all became more noticeable after the introduction of SO_2, NH_3, and NO with Hg^0 + O_2, resulting in a remarkable suppression of Hg^{2+} formation. The Hg^{2+} amount also distinctly decreased when H_2O was introduced with Hg^0 + O_2, while it was maintained at approximately 15 μg m^{-3} (Fig. 7b).

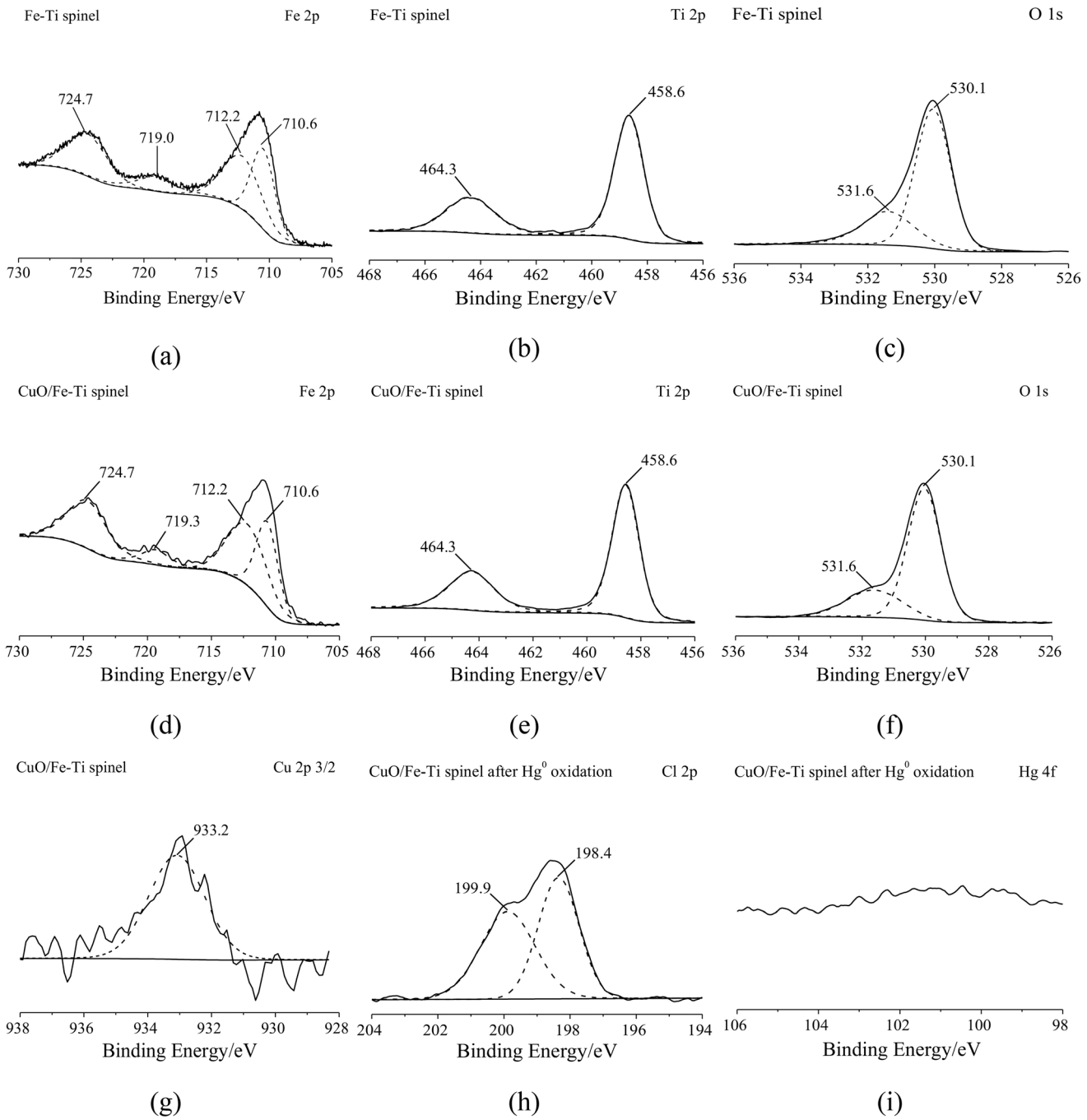

Fig. 3 XPS spectra of Fe–Ti, CuO/Fe–Ti, and CuO/Fe–Ti spinel after Hg^0 oxidation in the Fe 2p, Ti 2p, O 1s, Cu $2p_{3/2}$, Cl 2p, and Hg 4f spectral regions.

4. Discussion

4.1 Hg^0 oxidation mechanism

The potential mechanism of Hg^0 oxidation on CuO/Fe–Ti spinel predominantly followed the Mars–Maessen (*i.e.*, HgO is oxidized by gaseous HCl to $HgCl_2$),[37,38] Eley–Rideal (*i.e.*, gaseous Hg^0 is oxidized by Cl* radicals to $HgCl_2$),[38,39] Deacon (*i.e.*, gaseous Hg^0 is oxidized by gaseous Cl_2 to $HgCl_2$),[40,41] and Langmuir–Hinshelwood mechanisms.[42,43]

The pathway of Hg^0 oxidation on CuO/Fe–Ti spinel based on the Mars–Maessen mechanism is expressed as:[37,38,44]

$$Hg^0_{(g)} \rightarrow Hg^0_{(ad)} \quad (1)$$

$$Hg^0_{(ad)} + 2 \equiv M^{n+} + O^{2-} \rightarrow HgO_{(ad)} + 2 \equiv M^{(n-1)+} \quad (2)$$

$$HgO_{(ad)} + 2HCl_{(g)} \rightarrow HgCl_{2(g)} + H_2O \quad (3)$$

$$2 \equiv M^{(n-1)+} + \frac{1}{2}O_2 \rightarrow 2M^{n+} + O^{2-} \quad (4)$$

where M^{n+} is the high-potential species on the surface (*i.e.*, Cu^{2+} and Fe^{3+}).

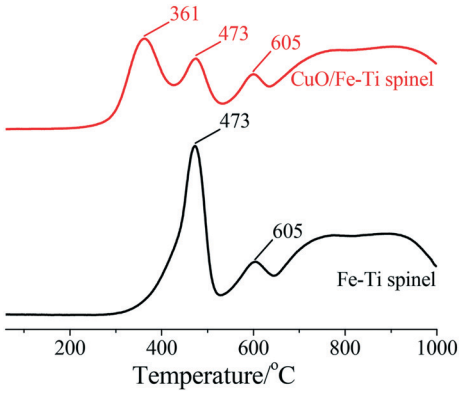

Fig. 4 H_2-TPR profiles of Fe–Ti and CuO/Fe–Ti spinel.

If Hg^0 oxidation on CuO/Fe–Ti spinel predominantly followed the Mars–Maessen mechanism, the formation of Hg^{2+} would depend upon the reaction between HgO and HCl (as suggested by reaction (4)). This indicates that the rate of Hg^{2+} formation for CuO/Fe–Ti spinel would not exceed that of HgO formation (*i.e.*, the rate of Hg^0 chemical adsorption). However, Fig. S4† shows that the Hg^0 oxidation rate of CuO/Fe–Ti was at least 15.7 times larger than its Hg^0 adsorption rate. This breaches the rationale of the Mars–Maessen mechanism. Hence, the Mars–Maessen mechanism was not dominant in Hg^0 oxidation on CuO/Fe–Ti spinel.

The pathway of Hg^0 oxidation on CuO/Fe–Ti spinel based on the Eley–Rideal mechanism is expressed as:[38,39,44]

$$HCl_{(g)} \rightarrow Cl^-_{(ad)} + H^+_{(ad)} \tag{5}$$

$$Cl^-_{(ad)} + \equiv M^{n+} \rightarrow Cl^*_{(ad)} + \equiv M^{(n-1)+} \tag{6}$$

$$Hg^0_{(ad)} + 2Cl^*_{(ad)} \rightarrow HgCl_{2(g)} \tag{7}$$

In accordance with reaction (7), the rate of Hg^0 oxidation for CuO/Fe–Ti spinel based on the Eley–Rideal mechanism is expressed as:

$$-\frac{d\left[HgCl_{2(g)}\right]}{dt}\Big|_{E-R} = k_1\left[Hg^0_{(g)}\right]\left[Cl^*_{(ad)}\right]^{\alpha} \tag{8}$$

where k_1, $[Cl^*_{(ad)}]$, $[Hg^0_{(g)}]$, and α are the rate constant of reaction (7), amounts of surface Cl* radicals and gaseous Hg^0, and order of reaction of reaction (7) based on the surface Cl* radical amount, respectively.

If Hg^0 oxidation on CuO/Fe–Ti spinel predominantly followed the Eley–Rideal mechanism, the rate of Hg^{2+} formation would dominantly depend upon the amounts of surface Cl* radicals and gaseous Hg^0 (as suggested by eqn (8)). Since the amount of gaseous Hg^0 was independent of the components, the interferences of the components with Hg^{2+} formation during the introduction of components + Hg^0 + O_2 into CuO/Fe–Ti spinel pretreated with O_2 + HCl would only be due to the decrease in the amount of surface Cl* radicals, which was predominantly related to the gradual consumption of surface Cl* radicals and the suppression of Cl* radical formation by the components. If surface Cl* radicals were gradually consumed by the components due to their reaction, the downward trend of the surface Cl* radical amount would become more noticeable during the introduction of components + Hg^0 + O_2 into CuO/Fe–Ti spinel pretreated with O_2 + HCl, resulting in a more noticeable decreasing trend of the Hg^{2+} concentration. However, Fig. 7b shows that the Hg^{2+} amount was maintained at approximately 15 μg m^{-3} when H_2O was introduced with Hg^0 + O_2 into CuO/Fe–Ti spinel pretreated with O_2 + HCl. This means that H_2O cannot react with Cl^* radicals, and the surface Cl* radicals would not be gradually consumed by H_2O. Meanwhile, H_2O barely interfered with the conversion of adsorbed Cl^- to Cl* radicals owing to its chemical inertness. This suggests that the formation of Cl* radicals would not be suppressed by H_2O (as suggested by reaction (6)). Therefore, the amount of surface Cl* radicals would not decrease after the addition of H_2O with Hg^0 + O_2, and there would be no interference with Hg^{2+} formation. However, Fig. 7b shows that Hg^{2+} formation was distinctly suppressed after the introduction

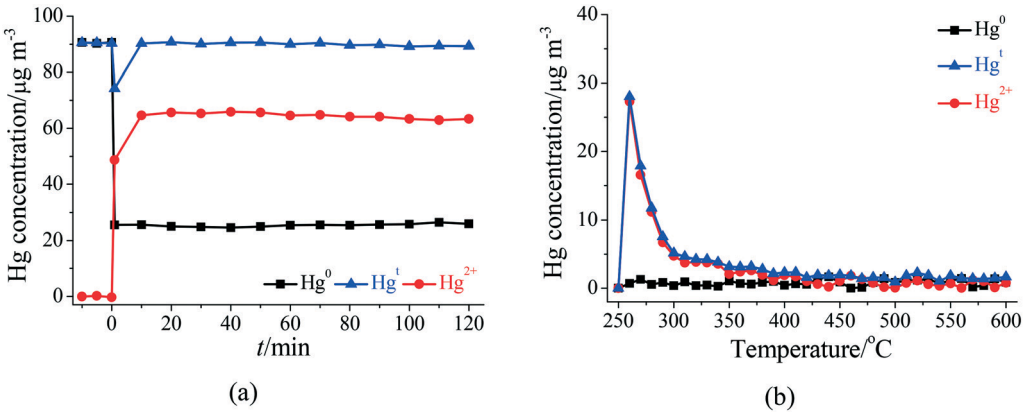

Fig. 5 (a) Amounts of Hg^0, Hg^t, and Hg^{2+} during Hg^0 oxidation on CuO/Fe–Ti spinel at 250 °C. (b) Hg-TPD profiles of CuO/Fe–Ti spinel after Hg^0 oxidation.

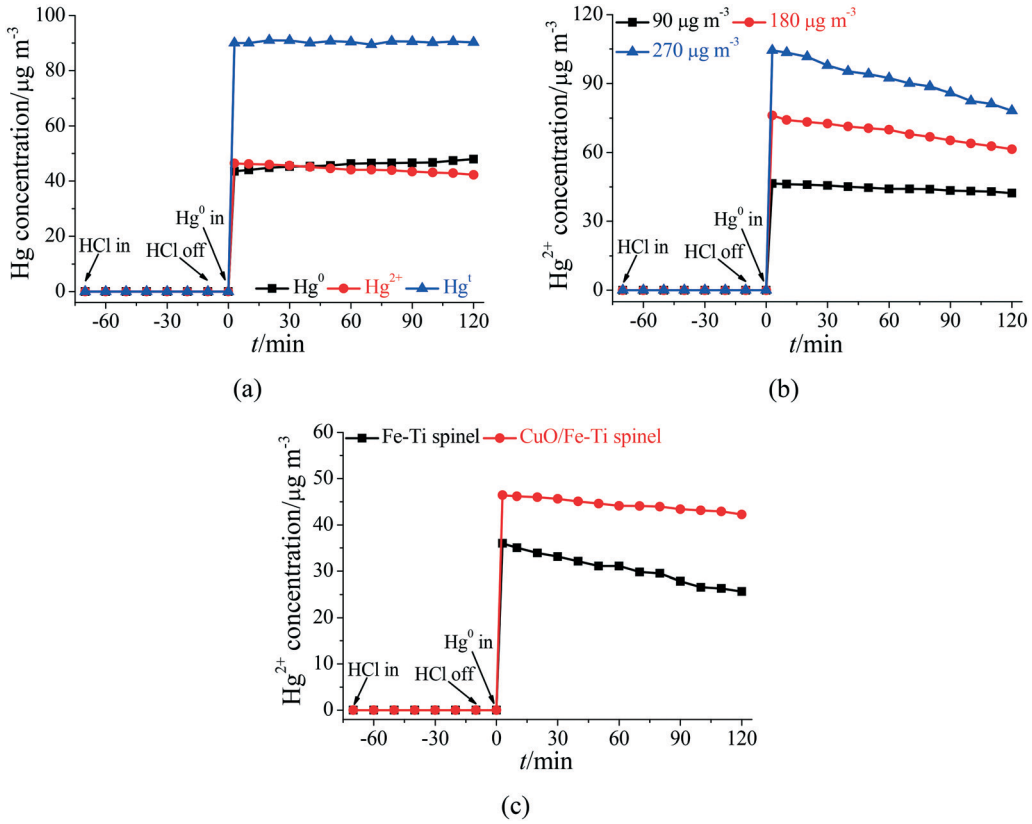

Fig. 6 (a) Transient reaction of the introduction of Hg^0 + O_2 into CuO/Fe–Ti spinel pretreated with O_2 + HCl at 250 °C. (b) Influence of the Hg^0 amount on Hg^{2+} formation during the introduction of Hg^0 + O_2 into CuO/Fe–Ti spinel pretreated with O_2 + HCl at 250 °C. (c) Hg^{2+} formation during the introduction of Hg^0 + O_2 into Fe–Ti and CuO/Fe–Ti spinel pretreated with O_2 + HCl at 250 °C.

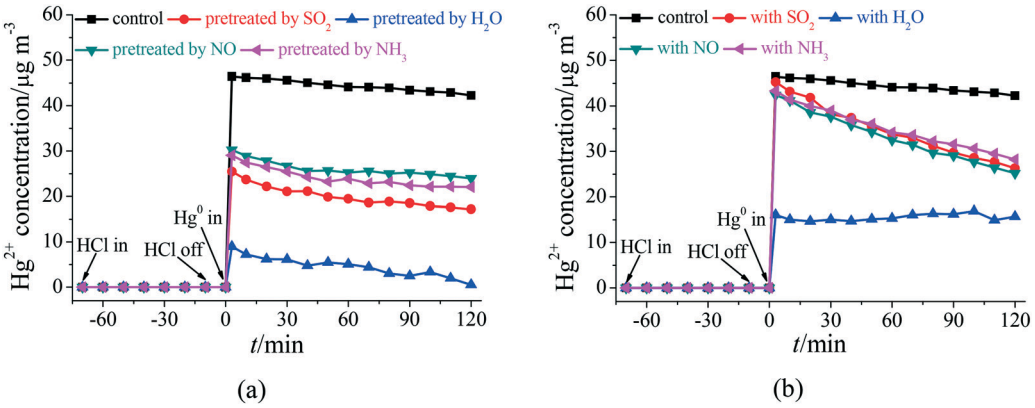

Fig. 7 Hg^{2+} formation during the introduction of (a) Hg^0 + O_2 into CuO/Fe–Ti spinel pretreated with components + O_2 + HCl and (b) components + Hg^0 + O_2 into CuO/Fe–Ti spinel pretreated with O_2 + HCl at 250 °C.

of H_2O + Hg^0 + O_2 into CuO/Fe–Ti spinel pretreated with HCl + O_2. This deviates from the result of the Eley–Rideal mechanism. Hence, the Eley–Rideal mechanism did not predominantly contribute to Hg^0 oxidation on CuO/Fe–Ti spinel.

The pathway of Hg^0 oxidation on CuO/Fe–Ti spinel based on the Deacon mechanism is expressed as:[40,41,44]

$$HCl_{(g)} \rightarrow Cl^-_{(ad)} + H^+_{(ad)} \quad (5)$$

$$Cl^-_{(ad)} + \equiv M^{n+} \rightarrow Cl^*_{(ad)} + \equiv M^{(n-1)+} \quad (6)$$

$$2Cl^*_{(ad)} \rightarrow Cl_{2(g)} \quad (9)$$

$$Hg^0_{(g)} + Cl_{2(g)} \rightarrow HgCl_{2(g)} \quad (10)$$

In accordance with reaction (10), the rate of Hg^0 oxidation for CuO/Fe–Ti spinel based on the Deacon mechanism is expressed as:

$$-\frac{d\left[HgCl_{2(g)}\right]}{dt}|_D = k_2\left[Hg^0_{(g)}\right]\left[Cl_{2(g)}\right]^{\beta} \quad (11)$$

where k_2, $[Cl_{2(g)}]$, and β are the rate constant of reaction (10), Cl_2 amount, and order of reaction of reaction (10) based on the Cl_2 amount, respectively.

If Hg^0 oxidation on CuO/Fe–Ti spinel predominantly followed the Deacon mechanism, its rate would dominantly depend upon the amounts of gaseous Cl_2 and Hg^0 (as suggested by eqn (11)). The decrease in the Cl_2 amount during the introduction of Hg^0 + O_2 into CuO/Fe–Ti spinel pretreated with O_2 + HCl only depended on reactions (5), (6), and (9), which were independent of the Hg^0 amount. Hence, the downward trend of the Hg^{2+} amount during the introduction of Hg^0 + O_2 into CuO/Fe–Ti spinel pretreated with O_2 + HCl would only be minimally related to the Hg^0 amount (as suggested by eqn (11)). However, Fig. 6b shows that the downward trend of the Hg^{2+} amount during the introduction of Hg^0 + O_2 into CuO/Fe–Ti spinel pretreated with O_2 + HCl became more notable when the Hg^0 amount increased. This contradicts the corollary of the Deacon mechanism. Hence, the Deacon mechanism was not predominant in Hg^0 oxidation on CuO/Fe–Ti spinel.

Since the other three mechanisms did not play major roles in Hg^0 oxidation on CuO/Fe–Ti spinel, the process dominantly followed the Langmuir–Hinshelwood mechanism, and its pathway is expressed as:[42–44]

$$Hg^0_{(g)} \rightarrow Hg^0_{(ad)} \quad (1)$$

$$HCl_{(g)} \rightarrow Cl^-_{(ad)} + H^+_{(ad)} \quad (5)$$

$$Cl^-_{(ad)} + \equiv M^{n+} \rightarrow Cl^*_{(ad)} + \equiv M^{(n-1)+} \quad (6)$$

$$Hg^0_{(ad)} + 2Cl^*_{(ad)} \rightarrow HgCl_{2(g)} \quad (12)$$

4.2 Promotion mechanism of CuO loading for Hg^0 oxidation on Fe–Ti spinel

In accordance with reaction (12), the rate of Hg^0 oxidation for CuO/Fe–Ti spinel based on the Langmuir–Hinshelwood mechanism is expressed as:

$$-\frac{d\left[HgCl_{2(g)}\right]}{dt}|_{L-H} = k_3\left[Hg^0_{(ad)}\right]\left[Cl^*_{(ad)}\right]^{\gamma} \quad (13)$$

where k_3, $[Hg^0_{(ad)}]$, and γ are the rate constant of reaction (12), amount of physically adsorbed Hg^0, and order of reaction of reaction (12) based on the surface Cl* radical amount, respectively.

In accordance with reaction (6), the Cl* radical formation rate of CuO/Fe–Ti spinel is expressed as:

$$-\frac{d\left[Cl^*_{(ad)}\right]}{dt} = k_4\left[Cl^-_{(ad)}\right]\left[M^{n+}\right]^{\delta} \quad (14)$$

where k_4, $[Cl^-_{(ad)}]$, $[M^{n+}]$, and δ are the rate constant of reaction (6), amounts of adsorbed Cl^- and surface M^{n+}, and order of reaction of reaction (6) based on the amount of surface M^{n+}, respectively.

Eqn (13) manifests that the rate of Hg^0 oxidation for CuO/Fe–Ti spinel was dominantly dependent upon the amounts of surface Cl* radicals and physically adsorbed Hg^0. This means that the promotion of Hg^0 oxidation on Fe–Ti spinel by CuO loading would be predominantly related to the promotion of the physical adsorption of Hg^0 or the Cl* radical formation.

Since the amounts of Hg^0 physically adsorbed on Fe–Ti and CuO/Fe–Ti spinel cannot be easily acquired directly using existing technologies, Hg^0 was chemically adsorbed onto Fe–Ti and CuO/Fe–Ti spinel (Fig. 8). It is common knowledge that the chemical adsorption of Hg^0 onto metal oxides predominantly followed the Mars–Maessen mechanism (*i.e.*, gaseous Hg^0 is first physically adsorbed on the surface, and is then oxidized by the high potential species to HgO).[45,46] Thus, the pathways of Hg^0 chemical adsorption onto Fe–Ti and CuO/Fe–Ti spinel are expressed as:[45,46]

$$Hg^0_{(g)} \rightarrow Hg^0_{(ad)} \quad (1)$$

$$Hg^0_{(ad)} + 2 \equiv M^{n+} + O^{2-} \rightarrow HgO_{(ad)} + 2 \equiv M^{(n-1)+} \quad (2)$$

$$2 \equiv M^{(n-1)+} + \frac{1}{2}O_2 \rightarrow 2M^{n+} + O^{2-} \quad (4)$$

In accordance with reactions (1) and (2), the Hg^0 adsorption rates of Fe–Ti and CuO/Fe–Ti spinel are expressed as:

$$-\frac{d\left[Hg^0_{(g)}\right]}{dt} = -\frac{d\left[Hg^0_{(ad)}\right]}{dt} = -\frac{d\left[HgO_{(ad)}\right]}{dt} = k_5\left[Hg^0_{(ad)}\right]\left[M^{n+}\right]^{\varepsilon} \quad (15)$$

where k_5 and ε are the rate constant of reaction (2) and order of reaction of reaction (2) based on the amount of surface M^{n+}, respectively. $[Hg^0_{(ad)}]$ is approximate to the product of the amount of adsorption sites (*i.e.*, $[\varphi]$) and its coverage ratio by physically adsorbed Hg^0 (*i.e.*, θ). θ was dominantly dependent upon the affinity of adsorption sites to gaseous Hg^0 and the amount of gaseous Hg^0. Hence, eqn (15) is transformed into:

$$-\frac{d\left[Hg^0_{(g)}\right]}{dt} = -\frac{d\left[Hg^0_{(ad)}\right]}{dt} = -\frac{d\left[HgO_{(ad)}\right]}{dt} = k_5\left[M^{n+}\right]^{\varepsilon}\theta[\varphi] \quad (16)$$

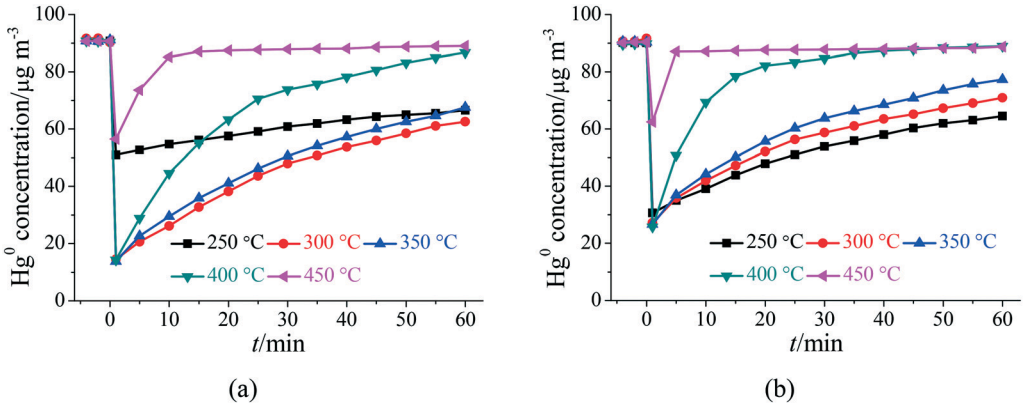

Fig. 8 Breakthrough curves of Hg^0 adsorption onto (a) Fe–Ti and (b) CuO/Fe–Ti spinel. Operating conditions: sorbent weight = 50 mg and MHSV = 6.0×10^5 cm^3 g^{-1} h^{-1}.

If the $[M^{n+}]$ of Fe–Ti and CuO/Fe–Ti spinel were both far larger than their $[\varphi]$, then the decrease in $[M^{n+}]$ during the adsorption of Hg^0 would not be taken into account. Hence, the $[\varphi]$ of Fe–Ti and CuO/Fe–Ti spinel during Hg^0 adsorption ($[\varphi]_t$) are approximately expressed as follows:

$$[\varphi]_t = [\varphi]_0 \exp(-k_5[M^{n+}]_0^{\varepsilon}\theta t) \tag{17}$$

Then, eqn (16) is converted into:

$$-\frac{d\left[Hg^0_{(g)}\right]}{dt} = k_5[M^{n+}]_0^{\varepsilon}\theta[\varphi]_0 \exp\left(-k_5[M^{n+}]_0^{\varepsilon}\theta t\right) = A \exp(-Bt) \tag{18}$$

where

$$A = k_5[M^{n+}]_0^{\varepsilon}\theta[\varphi]_0 \tag{19}$$

$$B = k_5[M^{n+}]_0^{\varepsilon}\theta \tag{20}$$

In accordance with eqn (19) and (20), $[\varphi]_0$ is obtained by:

$$[\varphi]_0 = A/B \tag{21}$$

The Hg^0 adsorption breakthrough curves of Fe–Ti and CuO/Fe–Ti spinel at 250–400 °C (Fig. 8) can be effectively fitted by eqn (18) ($R^2 > 0.980$), and their kinetic parameters are listed in Table 1. Hg^0 physical adsorption was generally an exothermic reaction; hence, Hg^0 physical adsorption onto Fe–Ti and CuO/Fe–Ti spinel would be suppressed with increasing temperature. Thus, the $[\varphi]$ of Fe–Ti and CuO/Fe–Ti spinel distinctly decreased as the temperature increased (Table 1). Since the $[\varphi]$ of Fe–Ti and CuO/Fe–Ti spinel were both very small at 450 °C, gaseous Hg^0 was difficult to be chemically adsorbed onto Fe–Ti and CuO/Fe–Ti spinel. Hence, the Hg^0 adsorption breakthrough curves of Fe–Ti and CuO/Fe–Ti spinel at 450 °C cannot be fitted well by eqn (18).

Table 1 shows that the values of $[\varphi]$ for Fe–Ti spinel were approximately 0.249 μmol g^{-1}, 0.218 μmol g^{-1}, 0.217 μmol g^{-1}, and 0.074 μmol g^{-1} at 250 °C, 300 °C, 350 °C, and 400 °C, respectively. However, Table 1 also shows that the values of $[\varphi]$ for CuO/Fe–Ti spinel were only approximately 0.194 μmol g^{-1}, 0.170 μmol g^{-1}, 0.111 μmol g^{-1}, and 0.032 μmol g^{-1} at 250 °C, 300 °C, 350 °C, and 400 °C, respectively. Hence, the $[\varphi]$ of CuO/Fe–Ti spinel was slightly smaller than that of Fe–Ti spinel, suggesting that the physical adsorption of Hg^0 onto Fe–Ti spinel was slightly suppressed after CuO loading, resulting in a worse Hg^0 adsorption activity of CuO/Fe–Ti spinel (Fig. 8). Therefore, the promotion of Hg^0 oxidation on Fe–Ti spinel by CuO loading predominantly resulted from the promotion of the formation of Cl* radicals.

Table 1 Kinetic parameters of Hg^0 adsorption onto Fe–Ti and CuO/Fe–Ti spinel

	Temperature °C	A/μg g^{-1} min^{-1}	B/min^{-1}	R^2	A/B/μmol g^{-1}
Fe–Ti spinel	250	0.421	0.0084	0.994	0.249
	300	0.771	0.0177	0.987	0.218
	350	0.791	0.0182	0.996	0.217
	400	0.785	0.0526	0.991	0.074
	450	—	—	—	—
CuO/Fe–Ti spinel	250	0.592	0.0152	0.984	0.194
	300	0.657	0.0193	0.991	0.170
	350	0.620	0.0278	0.987	0.111
	400	0.677	0.105	0.981	0.032
	450	—	—	—	—

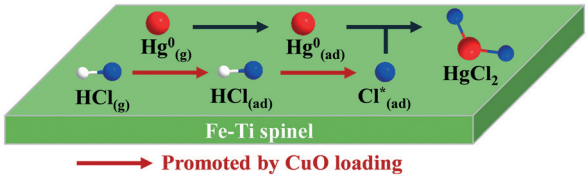

Fig. 9 Promotion mechanism of CuO loading for Hg^0 oxidation on Fe–Ti spinel.

The formation of Cl* radicals generally involved two steps: HCl adsorption (*i.e.*, reaction (5)) and the conversion of adsorbed Cl^- to Cl* radicals (*i.e.*, reaction (6)). Fig. 6c shows that the initial Hg^{2+} amount during the introduction of Hg^0 + O_2 into CuO/Fe–Ti spinel pretreated with O_2 + HCl was appreciably larger than that during its introduction into Fe–Ti spinel pretreated with O_2 + HCl. However, CuO loading slightly suppressed Hg^0 physical adsorption onto Fe–Ti spinel (Fig. 8). As suggested by eqn (13), the formed Cl* radical amount during the introduction of Hg^0 + O_2 into CuO/Fe–Ti spinel pretreated with O_2 + HCl was appreciably larger than that during its introduction into Fe–Ti spinel pretreated with O_2 + HCl, further demonstrating that the Cl* radical formation on Fe–Ti spinel was appreciably promoted after CuO loading. If Hg^0 oxidation played a leading role in the decrease of the surface Cl* radical amount during the introduction of Hg^0 + O_2 into Fe–Ti and CuO/Fe–Ti spinel pretreated with O_2 + HCl, the amount of adsorbed Cl^- would be approximately equivalent to that of formed Hg^{2+}. Fig. 6c indicates that the amount of Hg^{2+} formed during the introduction of Hg^0 + O_2 into CuO/Fe–Ti spinel pretreated with O_2 + HCl was appreciably larger than that during its introduction into Fe–Ti spinel pretreated with O_2 + HCl. This means that the amount of Cl^- adsorbed on CuO/Fe–Ti spinel was appreciably larger than that on Fe–Ti spinel. If the formation of Cl_2 (*i.e.*, the occurrence of reaction (9)) also contributed to the decrease in the amount of surface Cl* radicals during the introduction of Hg^0 + O_2 into Fe–Ti and CuO/Fe–Ti spinel pretreated with O_2 + HCl, the amount of adsorbed Cl^- would be approximately equal to the sum of the amounts of Cl_2 and Hg^{2+} formed. Since the formation of Cl* radicals on Fe–Ti spinel was appreciably enhanced after CuO loading, the amount of Cl_2 formed during the introduction of Hg^0 + O_2 into CuO/Fe–Ti spinel pretreated with O_2 + HCl would be appreciably larger than that during its introduction into Fe–Ti spinel pretreated with O_2 + HCl (as suggested by reaction (9)). Meanwhile, the amount of Hg^{2+} formed during the introduction of Hg^0 + O_2 into CuO/Fe–Ti spinel pretreated with O_2 + HCl was appreciably larger than that during its introduction into Fe–Ti spinel pretreated with O_2 + HCl (Fig. 6c). Hence, the sum of the amounts of Cl_2 and Hg^{2+} formed during the introduction of Hg^0 + O_2 into CuO/Fe–Ti spinel pretreated with O_2 + HCl was appreciably larger than that during its introduction into Hg^0 + O_2 into Fe–Ti spinel pretreated with O_2 + HCl. This also means that the amount of Cl^- adsorbed on CuO/Fe–Ti spinel was appreciably higher than that on Fe–Ti spinel. So anyway, HCl adsorption onto Fe–Ti spinel was appreciably promoted after CuO loading. Moreover, the percentage of Cl (5.1%) on CuO/Fe–Ti spinel was appreciably larger than that (2.8%) on Fe–Ti spinel, which resulted from the XPS analysis. This further demonstrates that HCl adsorption onto Fe–Ti spinel was appreciably enhanced after CuO loading. Furthermore, the H_2-TPR analysis manifests that the oxidation ability of CuO/Fe–Ti spinel was appreciably stronger than that of Fe–Ti spinel (Fig. 4); thus, the conversion of adsorbed Cl^- to Cl* radicals on CuO/Fe–Ti spinel was appreciably enhanced after CuO loading. Therefore, the promotion of the formation of Cl* radicals on Fe–Ti spinel by CuO loading was predominantly related to the promotion of both HCl adsorption and the conversion of adsorbed Cl^- to Cl* radicals (Fig. 9).

5. Conclusions

CuO/Fe–Ti spinel was exploited as a novel and high-activity SCR catalyst for Hg^0 oxidation as a co-benefit of NO abatement. Hg^0 oxidation on CuO/Fe–Ti spinel predominantly followed the Langmuir–Hinshelwood mechanism, and its rate was dominantly dependent upon the amounts of surface Cl* radicals and physically adsorbed Hg^0. Since HCl adsorption and the conversion of adsorbed Cl^- to Cl* radicals on Fe–Ti spinel were both appreciably enhanced after CuO loading, the formation of Cl* radicals on Fe–Ti spinel was appreciably promoted. Hence, Hg^0 oxidation on Fe–Ti spinel was appreciably promoted after CuO loading, although Hg^0 physical adsorption was slightly suppressed, and CuO/Fe–Ti spinel displayed outstanding Hg^0 oxidation activity, with the oxidation rate ranging from 6.8 to 8.7 $\mu g\ g^{-1}\ min^{-1}$, which was better than those of most other SCR catalysts. Meanwhile, CuO/Fe–Ti spinel displayed glorious SCR activity and high N_2 selectivity, which ensured the efficient removal of NO. In summary, CuO/Fe–Ti spinel may be used in SCR units to achieve the simultaneous removal of NO and Hg^0 from CFG.

Conflicts of interest

There are no conflicts to declare.

Acknowledgements

This study was supported by the National Natural Science Foundation of China (Grants 21906070 and 21777070), the Natural Science Foundation of Jiangsu Province (Grant BK20190616), and the Postgraduate Research & Practice Innovation Program of Jiangsu Province (Grant JNSJ19_015).

References

1 L. Chen, S. Liang, M. Liu, Y. Yi, Z. Mi, Y. Zhang, Y. Li, J. Qi, J. Meng and X. Tang, *Nat. Commun.*, 2019, **10**, 1–12.
2 J. Huang, S. Kang, M. Ma, J. Guo, Z. Cong, Z. Dong, R. Yin, J. Xu, L. Tripathee and K. Ram, *Environ. Sci. Technol.*, 2019, **53**, 6632–6639.

3 V. L. St. Louis, J. A. Graydon, I. Lehnherr, H. M. Amos, E. M. Sunderland, K. A. St. Pierre, C. A. Emmerton, K. Sandilands, M. Tate and A. Steffen, *Environ. Sci. Technol.*, 2019, **53**, 8017–8026.
4 D. G. Streets, H. M. Horowitz, Z. Lu, L. Levin, C. P. Thackray and E. M. Sunderland, *Atmos. Environ.*, 2019, **201**, 417–427.
5 J. Yang, Q. Li, M. Li, W. Zhu, Z. Yang, W. Qu, Y. Hu and H. Li, *Environ. Sci. Technol.*, 2020, **54**, 2022–2030.
6 J. Mei, P. Sun, C. Wang, Q. Zhang, Q. Hu and S. Yang, *Environ. Sci. Technol.*, 2020, **54**, 1992–2001.
7 Q. Yang, Z. Yang, H. Li, J. Zhao, J. Yang, W. Qu and K. Shih, *Chem. Eng. J.*, 2020, **398**, 125611.
8 H. Wang, W. Yu, X. Peng, Z. Chen, S. Wu, Q. Yu, W. Yang and J. Zhou, *Chem. Eng. J.*, 2020, **388**, 124220.
9 Z. Yang, H. Li, Q. Yang, W. Qu, J. Zhao, Y. Feng, Y. Hu, J. Yang and K. Shih, *Chem. Eng. J.*, 2020, **394**, 125022.
10 Y. Liao, D. Chen, S. Zou, S. Xiong, X. Xiao, H. Dang, T. Chen and S. Yang, *Environ. Sci. Technol.*, 2016, **50**, 10562–10569.
11 G. Li, Q. Wu, S. Wang, J. Li, X. You, S. Shao, M. Wen, L. Xu, Y. Tang and F. Wang, *Environ. Sci. Technol.*, 2020, **54**, 1889–1897.
12 F. Wang, G. Li, S. Wang, Q. Wu and L. Zhang, *Fuel*, 2020, **262**, 116506.
13 C. Li, D. Brewe and J. Lee, *Appl. Catal., B*, 2020, **270**, 118854.
14 Q. Wan, Q. Yao, L. Duan, X. Li, L. Zhang and J. Hao, *Environ. Sci. Technol.*, 2018, **52**, 2981–2987.
15 L. Zhao, C. Li, J. Zhang, X. Zhang, F. Zhan, J. Ma and G. Zeng, *Fuel*, 2015, **153**, 361–369.
16 J. Mei, P. Sun, X. Xiao, Q. Zhang, H. Zhao, Y. Guo and S. Yang, *J. Ind. Eng. Chem.*, 2019, **75**, 130–137.
17 J. Yang, Q. Yang, J. Sun, Q. Liu, D. Zhao, W. Gao and L. Liu, *Catal. Commun.*, 2015, **59**, 78–82.
18 A. Beretta, N. Usberti, L. Lietti, P. Forzatti, M. Di Blasi, A. Morandi and C. La Marca, *Chem. Eng. J.*, 2014, **257**, 170–183.
19 N. Yan, W. Chen, J. Chen, Z. Qu, Y. Guo, S. Yang and J. Jia, *Environ. Sci. Technol.*, 2011, **45**, 5725–5730.
20 C. Chen, W. Jia, S. Liu and Y. Cao, *J. Mater. Sci.*, 2018, **53**, 10001–10012.
21 S. Ali, L. Chen, Z. Li, T. Zhang, R. Li, S. U. H. Bakhtiar, X. Leng, F. Yuan, X. Niu and Y. Zhu, *Appl. Catal., B*, 2018, **236**, 25–35.
22 G. Yang, H. Zhao, X. Luo, K. Shi, H. Zhao, W. Wang, Q. Chen, H. Fan and T. Wu, *Appl. Catal., B*, 2019, **245**, 743–752.
23 S. Ma, X. Zhao, Y. Li, T. Zhang, F. Yuan, X. Niu and Y. Zhu, *Appl. Catal., B*, 2019, **248**, 226–238.
24 S. Yang, J. Li, C. Wang, J. Chen, L. Ma, H. Chang, L. Chen and N. Yan, *Appl. Catal., B*, 2012, **117**, 73–80.
25 Q. Zhang, J. Mei, P. Sun, H. Zhao, Y. Guo and S. Yang, *Ind. Eng. Chem. Res.*, 2020, **59**, 61–70.
26 S. Yang, Y. Guo, N. Yan, D. Wu, H. He, Z. Qu, C. Yang, Q. Zhou and J. Jia, *ACS Appl. Mater. Interfaces*, 2011, **3**, 209–217.
27 S. Xiong, X. Xiao, Y. Liao, H. Dang, W. Shan and S. Yang, *Ind. Eng. Chem. Res.*, 2015, **54**, 11011–11023.
28 H. Chang, Q. Wu, T. Zhang, M. Li, X. Sun, J. Li, L. Duan and J. Hao, *Environ. Sci. Technol.*, 2015, **49**, 12388–12394.
29 Y. Gao, Z. Zhang, J. Wu, L. Duan, A. Umar, L. Sun, Z. Guo and Q. Wang, *Environ. Sci. Technol.*, 2013, **47**, 10813–10823.
30 L. Zhao, C. Li, X. Zhang, G. Zeng and J. Zhang, *Catal. Sci. Technol.*, 2015, **5**, 3459–3472.
31 S. Zou, Y. Liao, S. Xiong, N. Huang, Y. Geng and S. Yang, *Environ. Sci. Technol.*, 2017, **51**, 3426–3434.
32 P. S. Bagus, C. J. Nelin, C. R. Brundle and S. A. Chambers, *J. Phys. Chem. C*, 2018, **123**, 7705–7716.
33 J. Mei, Y. Ke, Z. Yu, X. Hu, Z. Qu and N. Yan, *Chem. Eng. J.*, 2017, **320**, 124–134.
34 L. Kong, S. Zou, J. Mei, Y. Geng, H. Zhao and S. Yang, *Environ. Sci. Technol.*, 2018, **52**, 10003–10010.
35 J. Mei, C. Wang, L. Kong, P. Sun, Q. Hu, H. Zhao, Y. Guo and S. Yang, *J. Hazard. Mater.*, 2020, **381**, 120967.
36 L. Qi, Z. Sun, Q. Tang, J. Wang, T. Huang, C. Sun, F. Gao, C. Tang and L. Dong, *J. Hazard. Mater.*, 2020, **396**, 122459.
37 W. Chen, Y. Pei, W. Huang, Z. Qu, X. Hu and N. Yan, *Environ. Sci. Technol.*, 2016, **50**, 2564–2572.
38 S. Xiong, X. Xiao, N. Huang, H. Dang, Y. Liao, S. Zou and S. Yang, *Environ. Sci. Technol.*, 2017, **51**, 531–539.
39 Z. Liu, V. Sriram, C. Li and J. Lee, *Catal. Sci. Technol.*, 2017, **7**, 4669–4679.
40 C. He, B. Shen, G. Chi and F. Li, *Chem. Eng. J.*, 2016, **300**, 1–8.
41 S. Zhao, H. Xu, J. Mei, Y. Ma, T. Lou, Z. Qu and N. Yan, *Fuel*, 2017, **200**, 236–243.
42 B. Zhao, X. Liu, Z. Zhou, H. Shao and M. Xu, *Chem. Eng. J.*, 2016, **284**, 1233–1241.
43 Z. Xu, X. Lv, J. Chen, L. Jiang, Y. Lai and J. Li, *Chem. Eng. J.*, 2017, **308**, 1225–1232.
44 L. Zhao, C. Li, X. Zhang, G. Zeng, J. Zhang and Y. Xie, *Catal. Sci. Technol.*, 2015, **5**, 3459–3472.
45 W. Xu, A. Hussain and Y. Liu, *Chem. Eng. J.*, 2018, **346**, 692–711.
46 H. Xu, Z. Qu, C. Zong, W. Huang, F. Quan and N. Yan, *Environ. Sci. Technol.*, 2015, **49**, 6823–6830.

